A Semiempirical Cloudiness Parameterization for Use in Climate Models

KUAN-MAN XU AND DAVID A. RANDALL

Department of Atmospheric Science, Colorado State University, Fort Collins, Colorado

(Manuscript received 5 June 1995, in final form 15 April 1996)

ABSTRACT

Data produced from explicit simulations of observed tropical cloud systems and subtropical stratocumuli are used to develop a "semiempirical" cloudiness parameterization for use in climate models. The semiempirical cloudiness parameterization uses the large-scale average condensate (cloud water and cloud ice) mixing ratio as the primary predictor. The large-scale relative humidity and cumulus mass flux are also used in the parameterization as secondary predictors. The cloud amount is assumed to vary exponentially with the large-scale average condensate mixing ratio. The rate of variation is, however, a function of large-scale relative humidity and the intensity of convective circulations. The validity of such a semiempirical approach and its dependency on cloud regime and horizontal-averaging distance are explored with the simulated datasets.

1. Introduction

The treatment of clouds is one of the most complex tasks in developing global climate models (GCMs) because (i) they cannot be resolved by the conventional grid size used in GCMs; (ii) they can nonlinearly interact with radiative, dynamical, and hydrological processes on a wide range of timescales; and (iii) they act as one of the most important mechanisms for the vertical redistribution of momentum, sensible, and latent heat for the large scale. Among the most important cloud systems in the climate are the midlatitude frontal clouds, the subtropical stratus and stratocumulus, and the upper-tropospheric clouds associated with deep cumulus convection in the Tropics and summer midlatitudes. Midlatitude frontal clouds are the major source of precipitation associated with cyclones in the winter hemisphere. Subtropical stratus and stratocumulus are the major persistent phenomenon off subtropical continents and influence the earth's radiative energy budget due to their high albedos (Randall et al. 1984). The upper-tropospheric clouds can also significantly influence the radiative balance (Webster and Stephens 1980). They are closely associated with deep cumulus convection, which is the primary mechanism for transport of moisture from the planetary boundary layer (PBL) to the upper troposphere, especially in the Tropics and summer midlatitudes. Moist air detrained from cumulus towers forms horizontally extensive "anvil" clouds. These anvil clouds are a major component of stratiform precipitation associated with mesoscale convective systems (e.g., Houze 1977).

Inclusion of the aforementioned effects of the upper-tropospheric clouds and the linkage between deep cumulus convection and stratiform clouds in GCMs are two major challenges for climate modelers (Randall 1989). A consistent treatment of them has yet to emerge, although there is now an increased effort to improve the cloud formation parameterization. In most existing GCMs the treatment of large-scale stratiform clouds, that is, cloudiness and the radiative effects of these clouds on the large scale, is somewhat disconnected with that of deep cumulus convection. The stratiform cloudiness is usually estimated from a diagnostic relation based mainly on large-scale relative humidity with different complexities and details [see Xu and Krueger (1991) for a review and evaluation]. This is usually termed the *diagnostic* approach for cloud formation–dissipation processes. With such a diagnostic parameterization of cloudiness, the time change of cloudiness associated with anvil clouds and cirrus debris arising from cumulus activity might not be recognized at all through the gridscale variables of the GCM. For example, the long-lasting anvil clouds and cirrus debris may not be captured because the parameterized cloudiness is assumed to be zero once deep convection dissipates (Randall 1989; Randall et al. 1989). Therefore, the linkage between deep cumulus convection and stratiform clouds cannot be properly represented by the diagnostic approach.

To overcome the deficiencies mentioned above, a "prognostic" approach using prognostic equations for cloud water and/or cloud ice was pioneered by Sundqvist (1978). The advantages of such a parameterization are that (i) cloud formation and dissipation pro-

Corresponding author address: Dr. Kuan-Man Xu, Department of Atmospheric Science, Colorado State University, Fort Collins, CO 80523.
E-mail: kmxu@cumulus.atmos.colostate.edu

cesses can be represented, (ii) the latent heat effects and the radiative effects of clouds are physically linked, and (iii) a consistent coupling of the convective and stratiform cloud parameterizations can be achieved via treating the detrained condensed water from cumulus towers as a source of stratiform formation (Randall 1989; Tiedtke 1993; Fowler et al. 1996). The prognostic approach consists of two interrelated aspects: 1) the formulation of the sources and sinks of cloud water/ice associated with phase changes and the detrainment of condensed water from cumulus towers and 2) the parameterization of subgrid cloud amount or fractional cloudiness. The latter is the focus of this study. A companion paper (Xu and Randall 1996b) evaluates statistically based cloudiness parameterizations used in climate models.

In this study, subgrid cloud amount can be generally defined as the statistical distribution of cloud water and cloud ice on the subgrid scale. Such a definition of cloud amount encompasses not only the cloudy fractions of a grid cell but also thick and thin cloud patches. (The latter aspect will not be addressed in this study.) The major reasons for parameterizing fractional cloudiness are as follows. First, the small-scale distributions of liquid water and ice can have strong effects on radiative transfer. Second, microphysical transformations among water species are *local* or cloud-scale processes so that they must be formulated in terms of the local concentrations of cloud water/ice instead of the predicted grid-cell averaged concentrations. To the first order, these local concentrations are equal to the grid-cell averaged concentrations divided by the cloud amount. Third, subgrid cloud amount may affect the dynamics of convective clouds that produce much of the condensation through the interactions between convective and stratiform processes. For instance, Randall (1987) discussed the effects of fractional cloudiness on stratocumulus dynamics.

Two principal aspects should be emphasized in developing a cloudiness parameterization within the framework of the prognostic approach. First, a subgrid cloudiness parameterization should be physically based, as far as possible. Any such parameterization may have some empirical content but the empiricism should be introduced in a such a way that the formulation is universally applicable, that is, not tied to a particular cloud regime or a specific grid size of the GCMs. Second, since the mass of condensed water is predicted (e.g., Sundqvist 1978; LeTreut and Li 1988; Smith 1990; Ghan and Easter 1992; Fowler et al. 1996), the grid-averaged cloud water/ice mixing ratio itself is an obvious candidate for use as a predictor of subgrid cloud amount. This is the conceptual starting point for the approach proposed in this study. A major difficulty in developing such a cloudiness parameterization, however, arises from the lack of observations of the detailed, statistical properties of cloud fields. To fill the gap between observations and development of parameterizations, a cloud ensemble model (CEM) is used. CEMs cover a large horizontal area with a sufficiently small horizontal grid size to resolve individual clouds. They can provide many valuable datasets by simulating different cloud regimes in the atmosphere (e.g., Tao et al. 1987; Xu and Krueger 1991; Gregory and Miller 1989). CEMs are a very useful tool for the development of such an approach because they can provide detailed information of the mixing ratio of condensate and that of fractional cloud amount, as well as other large-scale predictors.

A main objective of the present study is, therefore, to develop a semiempirical formulation of subgrid cloud amount for use in climate models based on numerically simulated datasets using observed large-scale conditions. Even though it is not deduced from observations, it is derived from CEM simulations using a curve-fitting approach. Some aspects of simulated results can be verified with observed datasets. Two datasets will be used; one is the Global Atmospheric Research Program's (GARP's) Atlantic Tropical Experiment (GATE) and the other is the Atlantic Stratocumulus Transition Experiment (ASTEX). Ideally, many cloud regimes should be simulated in order to develop and evaluate a comprehensive parameterization. These two datasets, however, represent more than two distinct cloud regimes because many synoptic conditions are observed in each experiment. Therefore, the universal validity of the new parameterization should not arguably be an issue provided unique empiricism can be introduced based on the two simulated datasets.

2. Numerical simulations

The model used is the University of California, Los Angeles CEM, which is based on the two-dimensional (x and z) anelastic system of equations with Coriolis acceleration and a three-phase bulk microphysical parameterization (Krueger 1988; Xu and Krueger 1991; Krueger et al. 1995). A unique aspect of this model is that a third-moment closure is used for turbulence parameterization. This parameterization improves the simulation of boundary layer turbulence and the treatment of in-cloud turbulence (Krueger 1988). The three-phase microphysics is represented by a bulk parameterization based on Lin et al. (1983) and Lord et al. (1984) with recent modifications described by Krueger et al. (1995). The modified parameterization is able to realistically simulate the microphysical processes that occur in upper-tropospheric clouds. A radiation parameterization has been incorporated into the model (Xu and Randall 1995) based on the two-stream, broadband radiative transfer model developed by Harshvardhan et al. (1987). In addition, a turbulence-scale saturation parameterization (Chen 1991) is used for simulating stratus and stratocumulus but is not activated for simulating tropical cloud systems. In the latter case, subgrid cloudiness is diagnosed if the sum of

cloud-water and cloud-ice mixing ratio within a grid box is less than 1% of the saturation water-vapor mixing ratio, which is needed for radiation and turbulence-flux conversions in the model.

The CEM allows for the inclusion of different large-scale conditions, such as the large-scale vertical velocity, the horizontal advection of temperature and water-vapor mixing ratio, and the large-scale pressure gradient forces, such that different cloud regimes can be simulated (Xu and Krueger 1991; Xu et al. 1992). The cloud regimes in this study are tropical cloud systems and subtropical shallow clouds.

a. GATE simulation

The tropical cloud systems during Phase III of GATE have been simulated with observed large-scale data (Xu and Randall 1996a). The details of the simulation have been extensively compared with available observations. Figure 1 shows a comparison of the low-level and total cloud amounts between observation and simulation. The observed cloud amounts were derived from the whole-sky camera observations at four GATE ships (Holle et al. 1979). The whole-sky camera emulates single-point observations by ground observers, while simulated cloud amount is defined based on the integrated liquid water content of CEM columns as in satellite observations of cloud amount. The latter does not have the limitations of an observed one, as discussed by Xu and Krueger (1991), but it is numerically simulated. The low-level clouds are those occurring between the ground and 850-mb level. The simulated cloud amounts are spatially averaged over the entire domain and 3 h in time. The observed ones are also time averaged over 3 h.

The correlation coefficients between observed and simulated cloud amounts are 0.43 and 0.42 for low-level and total clouds, respectively. The low-level cloud amounts are well underestimated due to a combination of reasons. One is the model's failure to produce subgrid-scale shallow cumuli without using a subgrid cloudiness parameterization, and the other is the different definitions of cloud fractions (Xu and Randall 1996a). The small correlation coefficients can also be attributed to the phase differences between simulated and observed convective activities and the lack of sufficiently large temporal fluctuations of the simulated cloudiness (Xu and Randall 1996a).

b. ASTEX simulation

The stratus and stratocumulus are simulated with large-scale data for a selected period during ASTEX. The ASTEX was intended to observe the transition between stratus and stratocumulus and took place in the Atlantic Ocean off the Portuguese coast in the summer of 1992 (Albrecht et al. 1995b). The simulation covers a five-day period between 17 and 22 June. The large-scale input data were analyzed by the European Centre for Medium-Range Weather Forecasts (ECMWF; Bretherton et al. 1995). The observed large-scale horizontal advection of heat and moisture, large-scale vertical velocity, geostrophic wind components, and sea surface temperature were imposed on the model. The data are averaged over a 2.5 degree × 2.5 degree square area centered at (32.5°N, 21.25°E) and are available every 6 h.

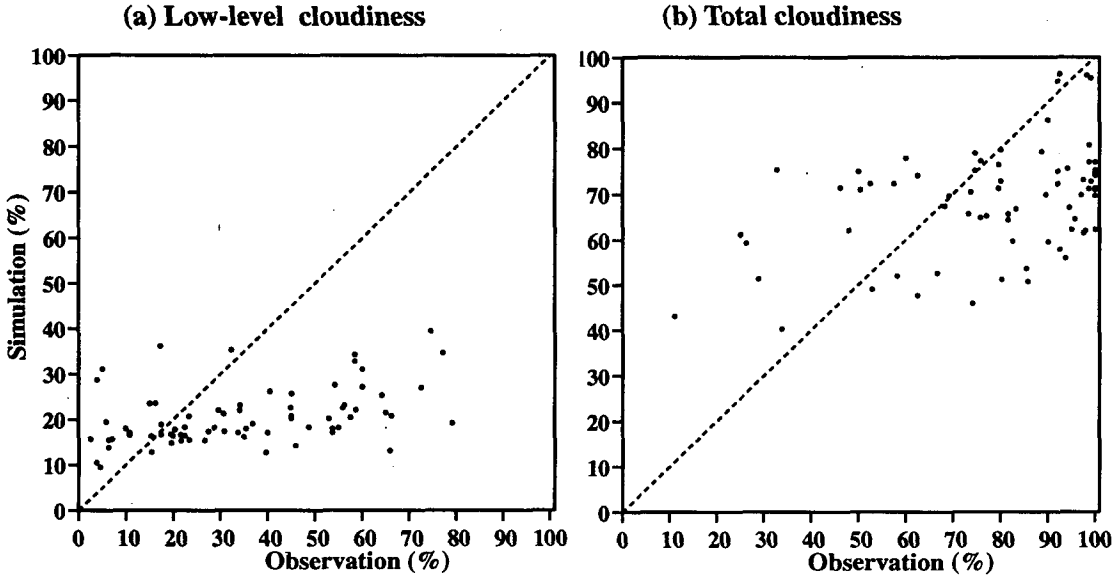

FIG. 1. Comparison between observed and simulated (a) low-level and (b) total cloud amount for the GATE Phase III. The observed cloud amounts are based on the whole-sky camera observations of Holle et al. (1979).

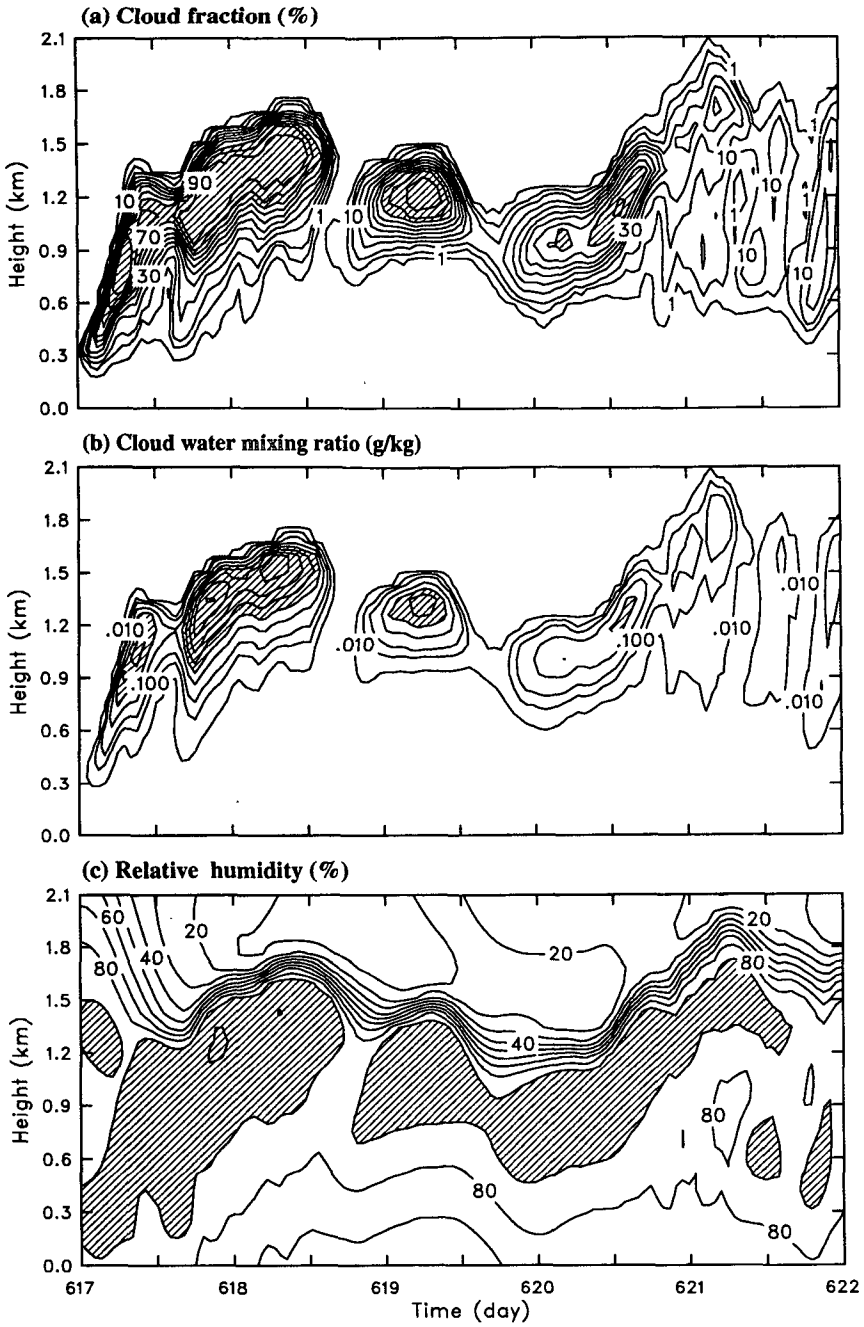

FIG. 2. Time–height cross section of (a) cloud fraction, (b) cloud water mixing ratio, and (c) relative humidity for the ASTEX simulation. The contour intervals are 10% in (a) and (c), 0.1 g kg^{-1} in (b). In (a) 1% and 5% contours are added, while 0.01 and 0.05 g kg^{-1} contours are added in (b).

In this simulation, the ice-phase microphysics parameterization is turned off because the modeled clouds do not reach the 0°C level. A flux-corrected transport algorithm (Grabowski and Smolarkiewicz 1990) is used to advect liquid-water static energy and total water mixing ratio. The horizontal domain size is 128 km with a grid size of 2 km. The domain depth is 3.6 km with a uniform spacing of 80 m. The time step is 4 s.

Simulated results related to this study are briefly presented here. Figure 2 shows time–height cross sections of domain-averaged, hourly cloud fraction, cloud water mixing ratio, and relative humidity. It is apparent that

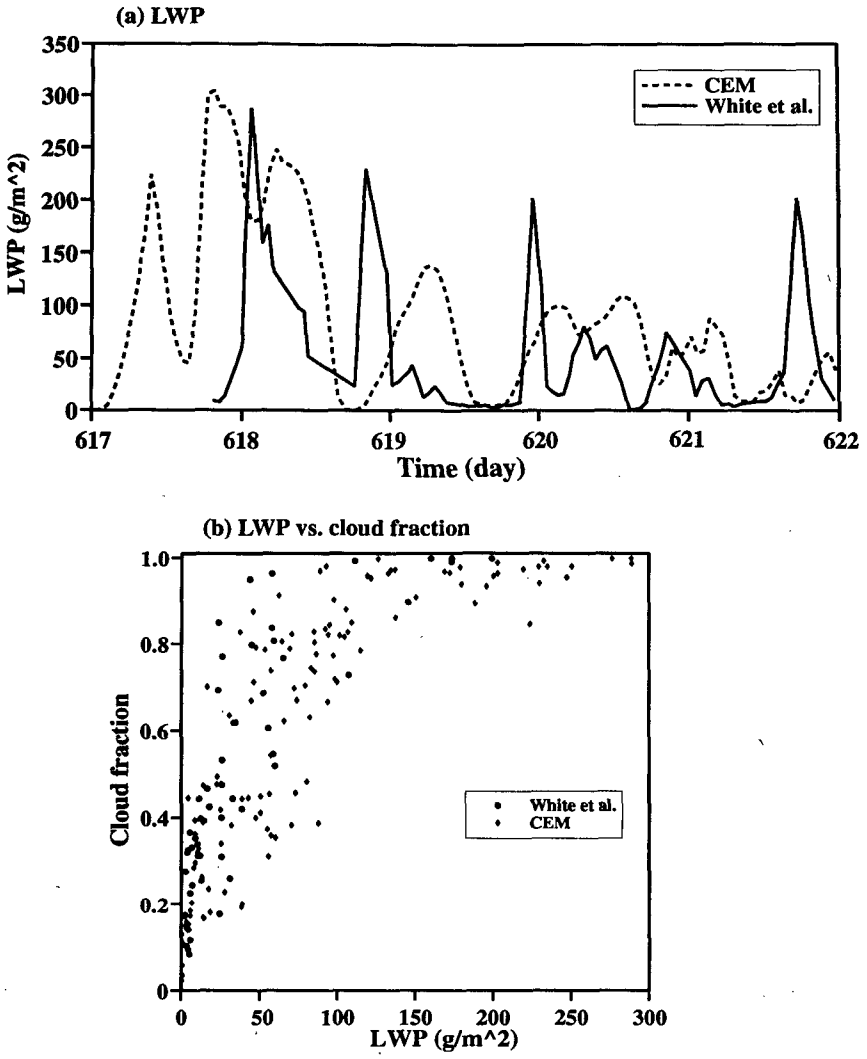

FIG. 3. (a) Time series of liquid water paths from observation and simulation between 17 and 22 June and (b) scatterplot of liquid water path vs cloud fraction from observation and simulation. The observations are based on White et al. (1995).

the cloud fraction (Fig. 2a) varies greatly and simultaneously with the cloud water mixing ratio (Fig. 2b). As expected, the cloud-top height varies with the inversion (Fig. 2c). The intensity of the inversion increases as the cloud fraction increases except for the initial model spinup. The diurnal variation of simulated clouds is clearly present with minima appearing in the afternoon and maxima in the early morning. During the last 30 h of the simulation, cumulus clouds dominate due to relatively strong upward motion (not shown). Another feature in Fig. 2 is that clouds develop in the moist portion (shaded areas in Fig. 2c) of the mixed layer. The relative humidity is relatively small when cumulus clouds develop on 21 June 1992.

Figure 3a shows a time series of simulated and observed liquid water paths (LWPs). The observations are based on White et al. (1995). The single-point, hourly observations were obtained from R/V *Malcolm Baldrige,* which moved with time (between 31.5° and 36.5°N, and between 21.5° and 26.5°E) in an area slightly west of the center of the 2.5 degree × 2.5 degree square. The observed LWPs shown in Fig. 3a were smoothed. The maxima of unsmoothed LWPs were as high as 400 g m^{-2} and were 10 times higher than the preceding or succeeding observations. Although the time series of LWPs agree poorly, the magnitude of simulated LWPs agrees reasonably well with that of the observed LWPs. The poor agreement is probably related to the fact that 1) single-point observations are not representative of an areal average, 2) temporal and spatial resolutions of ECMWF analyzed data are not adequate (Bretherton et al. 1995), and 3) the 2D

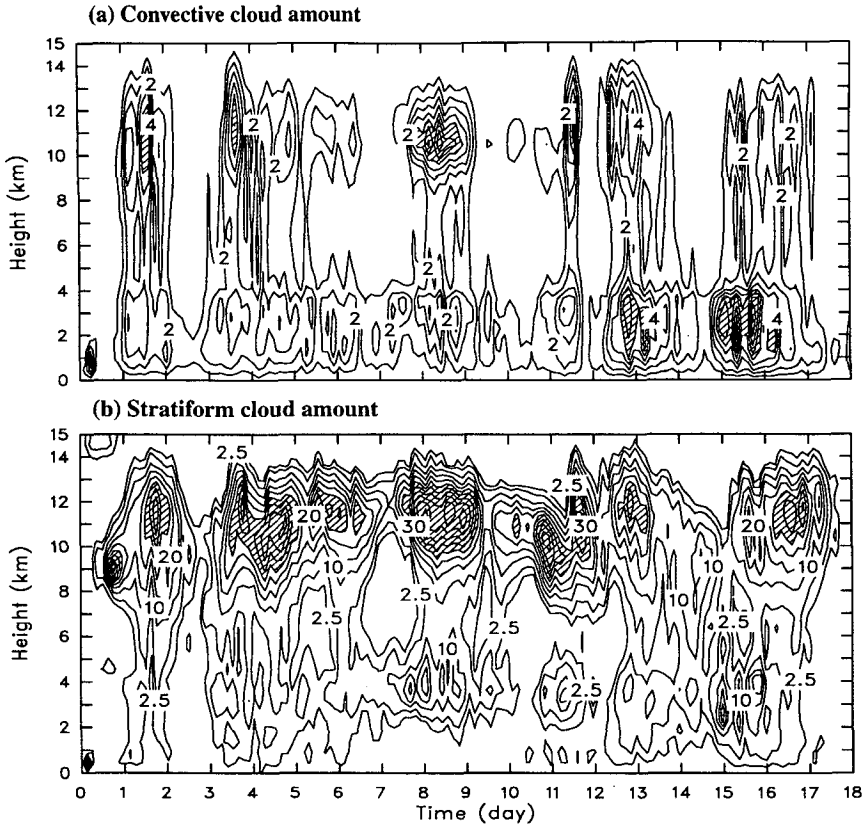

FIG. 4. Time–height cross sections of (a) convective and (b) stratiform cloud amounts for a GATE simulation. The contour intervals are 1% and 5% in (a) and (b), respectively. A 2.5% contour is added in (b). Contours over 5% and 25% are hatched in (a) and (b), respectively.

model may have some deficiencies. The last might not be the reason because of the good agreement shown in Fig. 3b; that is, the scatter of LWP versus cloud fraction is comparable between observation and simulation. The observed data used in Fig. 3b cover the entire ASTEX period except for missing data and are time averaged over 6 h. The simulated data are time averaged over 1 h and spatially over the domain. In summary, results shown in Fig. 3 give some confidence in the model.

3. Analysis procedure

The analysis procedure adopted in the present study is identical to that in Xu and Krueger (1991) except for the partitioning of convective and stratiform cloudinesses. A brief description is as follows. Instantaneous cloud amount within each grid box is time averaged over 3 h and spatially over the entire CEM domain or selected subdomains (64, 128, 256, and 512 km) to obtain the "large-scale" fractional cloudiness. (The time average is 1 h for the ASTEX simulation.) Any large-scale variable is similarly averaged. Xu and Krueger (1991) further divided the total cloud amount into convective (C_c) and stratiform components (C_s) using the cloud mass flux deviation at a given level as the criterion. This method does not give a coherent vertical structure of convective clouds. In the present study, an entire grid column is classified as either convective or stratiform following Xu (1995). The horizontal distribution of the maximum cloud draft strength ($|w_{\max}|$) below the melting level in a CEM grid column is used as a primary variable for partitioning. Details of the partitioning method were described in Xu (1995). Briefly, convective regions include those with large $|w_{\max}|$ and/or large surface precipitation rate, as well as those of nonprecipitating shallow convection. Stratiform regions consist of the remaining grid columns with liquid/ice water.

As discussed in Xu (1995), convective updrafts can sometimes be spuriously classified as stratiform regions due to vertical tilting of clouds. Therefore, an additional criterion has been added to roughly eliminate strong updrafts in the stratiform regions, that is, if the vertical velocity at any grid level is greater than 2 m s^{-1}. The impact due to the additional criterion is very small since the difference in the domain-averaged cloudiness is less than 2%. It does, however, affect the

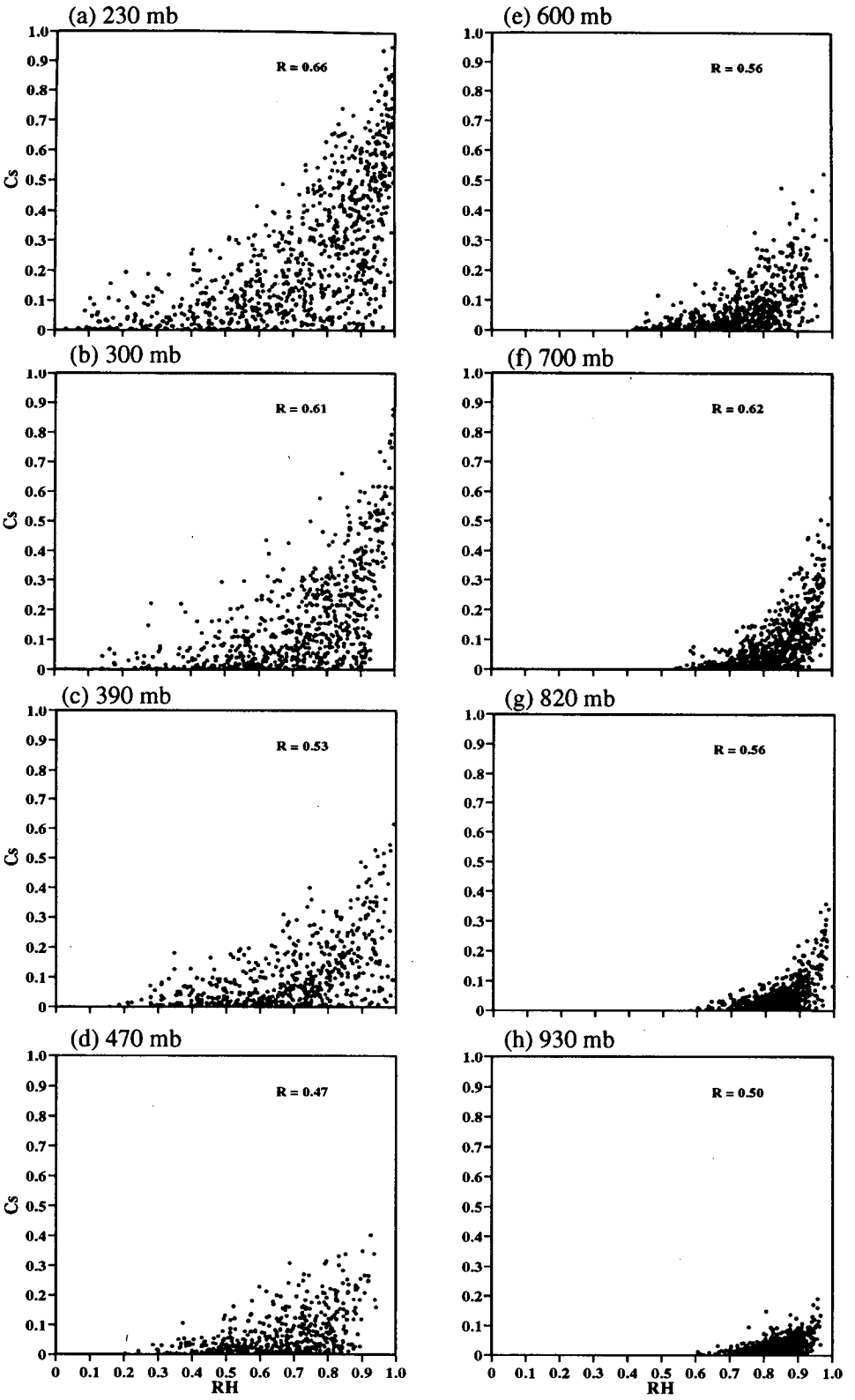

FIG. 5. Scatterplot of large-scale relative humidity vs stratiform cloud amount at selected levels for the 64-km subdomain of a GATE simulation. In each panel, R is the correlation coefficient between RH and cloud amount.

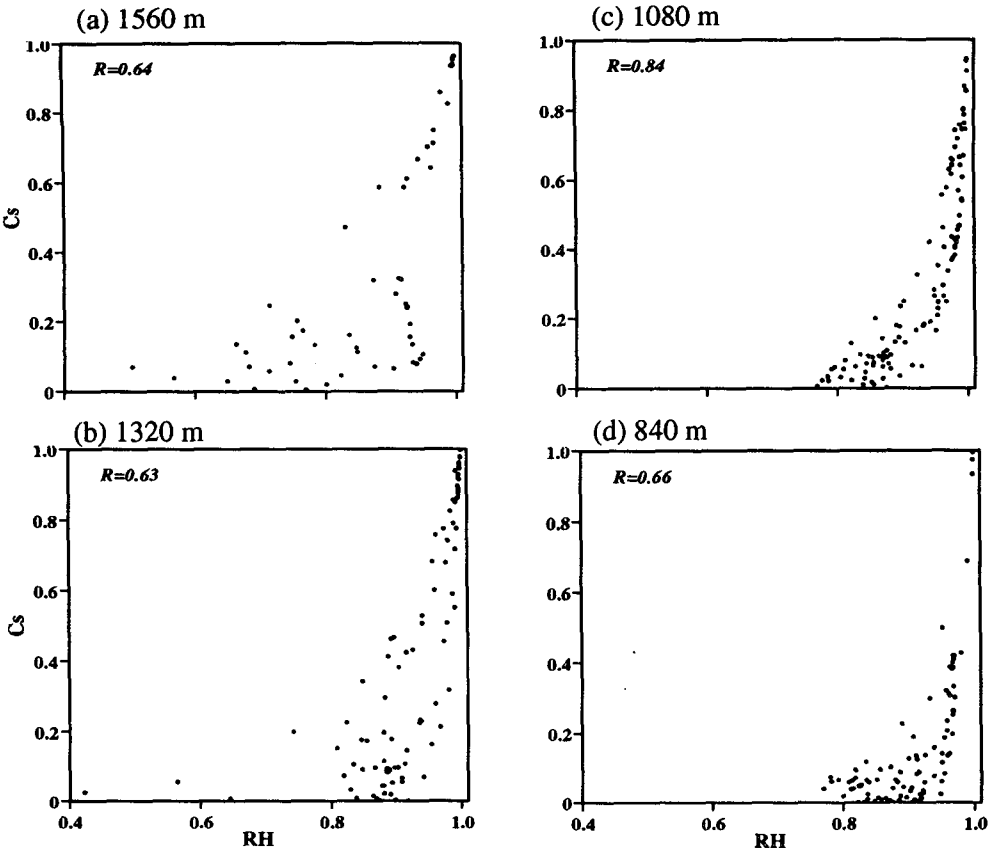

FIG. 6. Same as Fig. 5 except for the ASTEX simulation.

variances calculated to evaluate the probability density function (PDF) based approach in the companion paper (Xu and Randall 1996b) because strong drafts in the stratiform regions dominate the variances.

Figure 4 shows time–height cross sections of simulated C_s and C_c from the GATE simulation, between 1 and 18 September, to give insight into the partitioning method. The convective cloud amounts are generally less than 6% at all levels except for (i) the lowest 4 km on 13 and 16 September and (ii) the upper troposphere on 9 and 10 September. Shallow convection occurs in the lowest 4 km, more or less, for the entire simulation period. Deep convection appears only during certain periods, which is consistent with observations. The maxima of C_s are, as expected, much larger than those of C_c, especially in the upper troposphere (Fig. 4). The maxima of C_s generally occur in the upper troposphere when deep cumulus convection is active (Fig. 4b), for example, on 5 and 12 September. There is, however, a C_s maximum in the lower troposphere on 16 September, which precedes the occurrence of deep cumulus convection. Another feature is that C_s in the middle troposphere is generally very small even when deep convection is very active, for example, on 12 September. Overall, upper-tropospheric clouds associated with deep convection are, as expected, the dominant cloud type in the GATE simulation.

4. What determines fractional cloud amount?

In order to be useful in a GCM context, fractional cloudiness should be related to large-scale variables such as large-scale RH, grid-averaged mixing ratio of condensates and convective intensity. Since these variables are more or less interdependent, it is not likely that a single regression relationship using all correlated variables to parameterize fractional cloud amount is appropriate. Physical reasoning should be applied to formulate a cloudiness parameterization that should be independent of the grid size of a climate model and of the different cloud regimes. A few large-scale predictors are first examined to gain insight into the factors for determining fractional cloud amount.

a. RH as a predictor

As mentioned earlier, large-scale RH is the most frequently used variable for determining stratiform cloud amount in existing diagnostically based parameterizations (e.g., Smagorinsky 1960; Slingo 1980, 1987; Al-

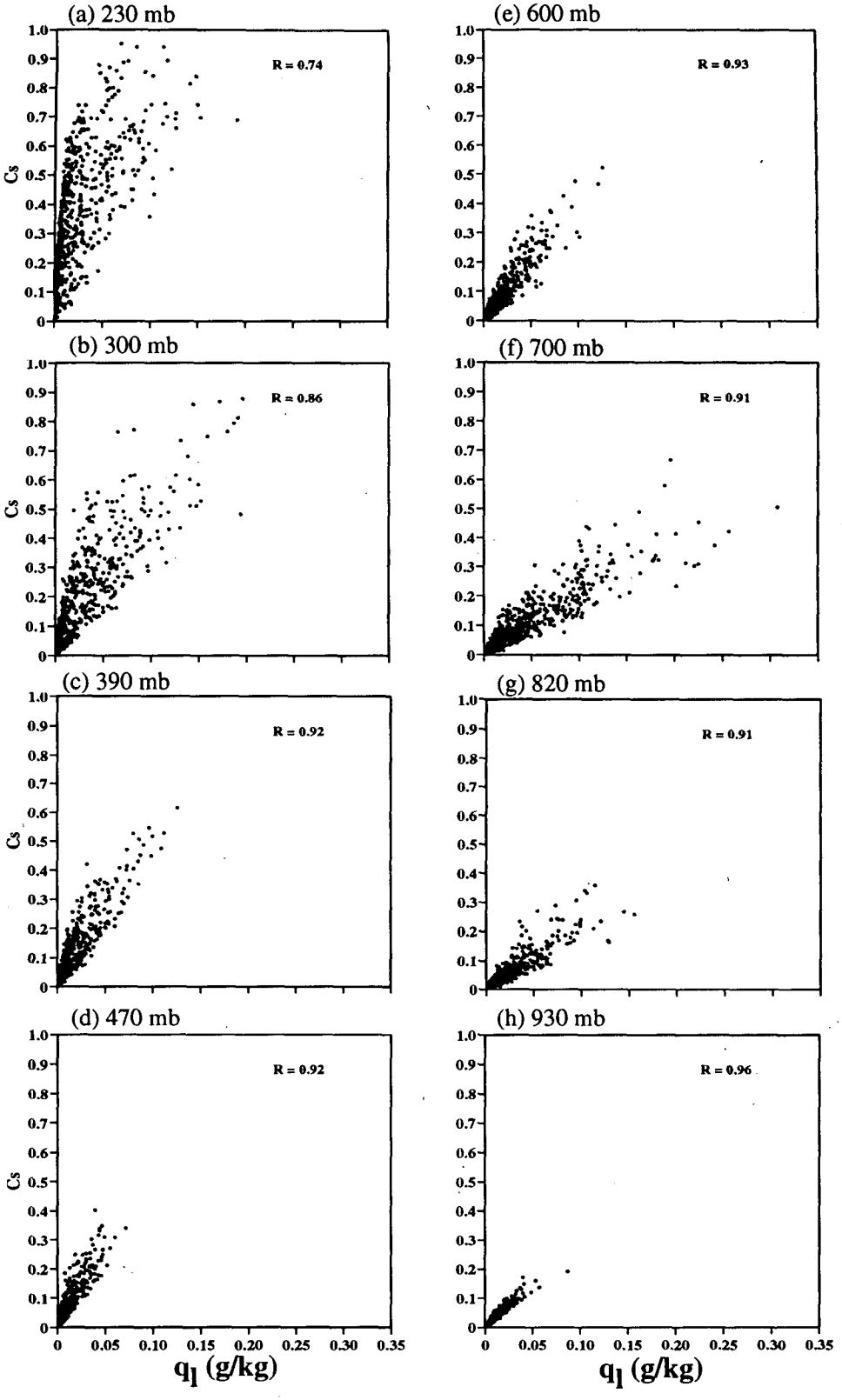

FIG. 7. Scatterplot of grid-averaged cloud water + ice mixing ratio vs stratiform cloud amount at selected levels for the 64-km subdomains of a GATE simulation. In each plot, R is the correlation coefficient between $\bar{q}_l$ and C_s.

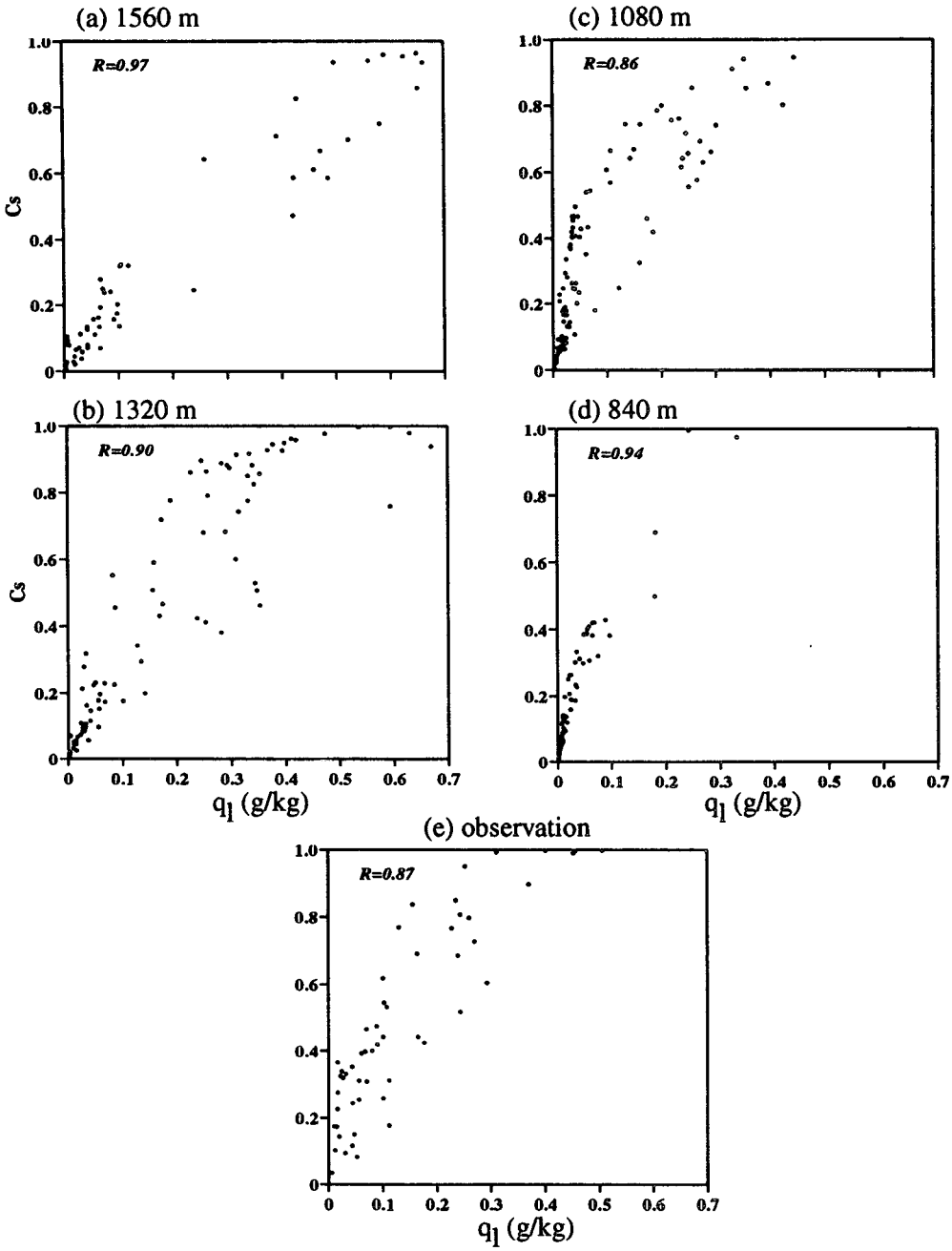

FIG. 8. Same as Fig. 7 except for the ASTEX simulation and observation.

brecht 1981; Sundqvist 1978; Walcek 1994). Figure 5 shows scatterplots of RH versus C_s at selected levels of the 64-km subdomains of the GATE simulation. Here, RH is calculated from the subdomain-averaged temperature and water vapor mixing ratio. The subdomain-averaged cloud-water and cloud-ice mixing ratios are also used if cloud water and cloud ice coexist (in the temperature range of −40° to 0°C). As seen from Fig. 5, there is some correlation between RH and C_s. The correlation coefficient ranges from 0.47 to 0.66 for the levels shown in Fig. 5. Another feature is that the range of RH variation for a given C_s is relatively small in the lower troposphere, which is related to the small variation of clear-region averaged RHs (Xu and Randall 1996b).

For a given RH, C_s can vary greatly, especially in the middle and upper troposphere. The range of the C_s variation for a given RH in the upper troposphere is

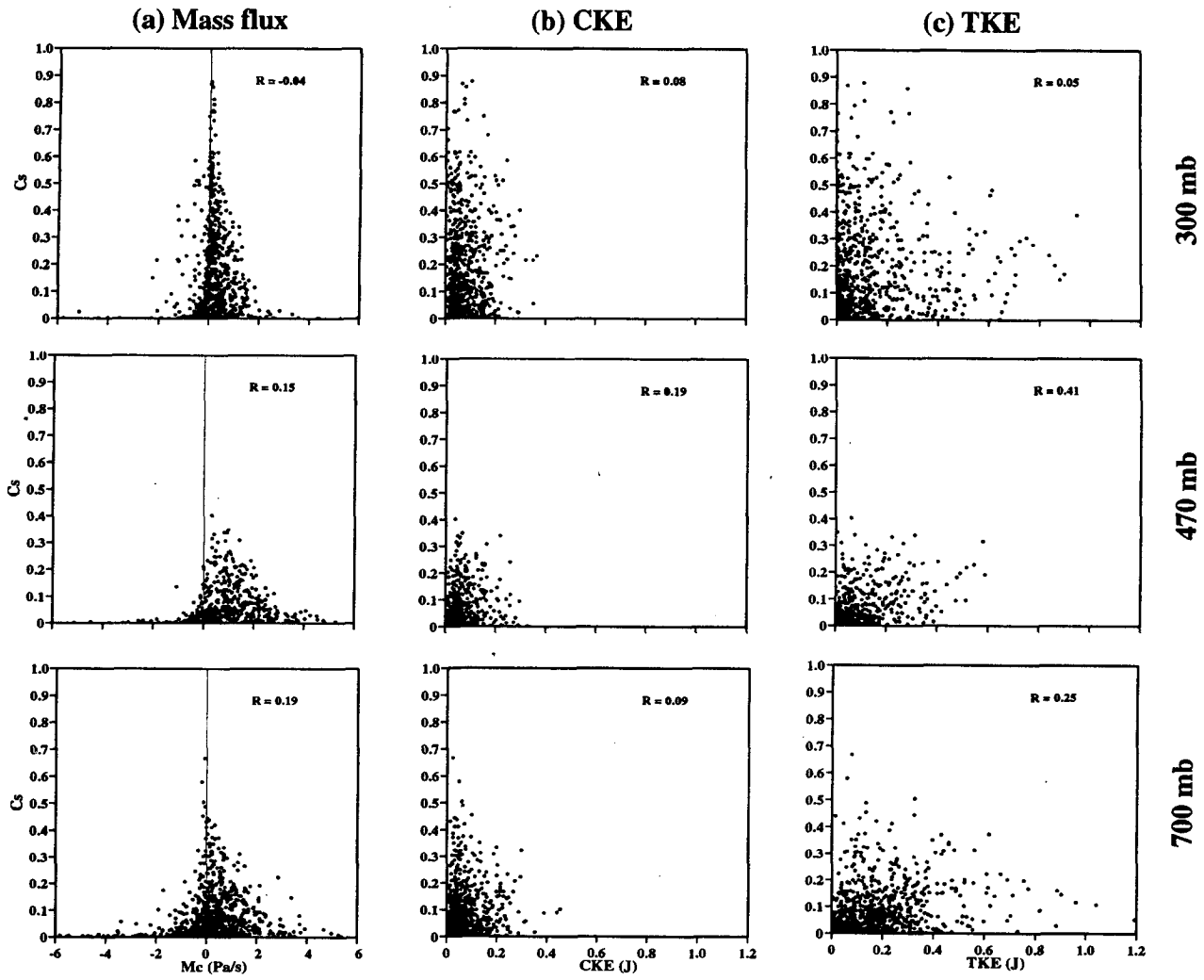

FIG. 9. Scatterplot of stratiform cloud amount vs cloud mass flux, cloud-scale vertical kinetic energy; and turbulence kinetic energy at 300-, 470-, and 700-mb levels for the 64-km subdomain of a GATE simulation. Here R is the correlation coefficient between predictor and cloud amount.

extremely large in spite of the high correlation coefficient (0.61 and 0.66 at 300-mb and 230-mb levels, respectively). The large variation is mainly related to the presence of different amounts of cloud water/ice for a given RH; the larger the amount of cloud water/ice, the larger the cloud amount that can be produced (see section 4e). For a given C_s, the variation of RHs may be related to the different intensities of deep convection (see section 4e) because deep convection tends to warm and dry the environment. It reduces the clear-region RHs and thus the subdomain-averaged RHs. In addition, Fig. 5 shows that there is no unique threshold RH for zero C_s at any level and it is also highly dependent on height, consistent with results shown in Xu and Randall (1996b). Therefore, existing RH-based cloudiness parameterizations, which use a single threshold RH at any level, are not universally valid. These results are consistent with those in Xu and Krueger (1991), although the methods for partitioning C_s and C_c are slightly different.

Figure 6 shows scatterplots of RH versus C_s at four selected levels in the upper portion of the boundary layer for the ASTEX simulation. The correlation coefficients range from 0.63 to 0.84 at these four levels, which are higher than those of GATE data. The most noticeable features in Fig. 6 are the steep slope of the regression line and the large scatter for a given RH. The large scatter is mostly related to stratocumuli in the late period of the simulation (Fig. 2a). The main point from Fig. 6 is that the predicted fraction of stratus and stratocumulus could be very sensitive to the errors in RH with an RH-based parameterization.

The results shown in Fig. 6 are consistent with recent observational studies by Bretherton et al. (1995) and

TABLE 1. Correlation coefficients between stratiform cloud amount and updraft mass flux (M_c) in convective regions, and between stratiform cloud amount and total mass flux in stratiform regions (M_s) for four subdomain sizes and selected levels.

Height (mb)	64 km		128 km		256 km		512 km	
	M_c	M_s	M_c	M_s	M_c	M_s	M_c	M_s
230	*0.47*	0.16	*0.56*	0.11	*0.63*	0.02	*0.63*	−0.28
300	0.21	*0.50*	0.22	*0.45*	0.18	0.34	0.07	0.15
390	0.22	*0.59*	0.19	*0.51*	0.18	*0.44*	0.07	0.31
470	0.18	*0.63*	0.15	*0.58*	0.12	*0.49*	−0.02	0.32
600	0.14	*0.49*	0.17	*0.43*	0.14	0.32	−0.03	0.22
700	0.18	0.20	0.21	0.15	0.22	0.11	0.04	0.17
820	0.29	0.14	0.32	0.10	0.31	0.09	0.14	0.14
930	*0.52*	0.03	*0.55*	−0.05	*0.62*	−0.07	*0.48*	−0.12

Albrecht et al. (1995a). Bretherton et al. (1995) showed that the RH in the upper boundary layer has statistically significant skill for predicting cloud fraction, with correlation coefficients between cloud fraction and RH in the range of 0.5–0.8 at three stations during ASTEX. They, however, pointed out that a 5%–10% low bias in RH in the upper boundary layer could cause a substantial reduction in cloudiness. Albrecht et al. (1995a) reached a similar conclusion with additional datasets.

b. $\bar{q}_l$ as a predictor

Figure 7 shows scatterplots similar to those in Fig. 5 except for the subdomain-averaged cloud water + ice mixing ratio $\bar{q}_l$ versus C_s. Here, $\bar{q}_l$ excludes the contribution from the convective regions. As mentioned in the introduction, $\bar{q}_l$ is a primary predictor for C_s to be examined in the present study. Major features appearing in Fig. 7 are as follows. The stratiform cloud amount, by and large, increases as $\bar{q}_l$ increases. The correlation coefficient between C_s and $\bar{q}_l$ (from 0.74 to 0.96) is much higher than that between C_s and RH at any level. This suggests that $\bar{q}_l$ may be a better predictor for C_s than RH.

Stratiform cloud amount increases almost linearly with $\bar{q}_l$, especially when $\bar{q}_l$ is small. When $\bar{q}_l$ is large, the variation of C_s with $\bar{q}_l$ becomes slower since the upper limit of C_s is 1. On the other hand, the scatter becomes larger as $\bar{q}_l$ increases (e.g., Figs. 7a,b, and f). The larger scatter of C_s for a given $\bar{q}_l$ suggests that additional large-scale predictors are needed to determine the different degree of C_s variation with respect to $\bar{q}_l$. In addition, the slopes of the regression lines become slightly steeper as the height increases. This may be related to the phase change of clouds from liquid to ice. In other words, a smaller amount of ice water can cover a larger cloud area than a larger amount of liquid water in the lower troposphere because the saturation mixing ratios differ significantly. This aspect will be further examined in section 5.

A simple explanation for the high correlation between $\bar{q}_l$ and C_s is that C_s represents the statistical distribution of cloud water and cloud ice on the subgrid scale. When an ensemble of clouds is included in the averaging, such a relationship between $\bar{q}_l$ and C_s is expected. This point will be more evident when results for larger averaging distances are examined in section 4d. Obviously, deviations from this relationship may be large for a single cloud or a small subdomain averaging because stratiform clouds are not necessarily horizontally homogeneous. The inhomogeneity tends to reduce C_s (section 4c).

If $\bar{q}_l$ can be used as a predictor for C_s, one has to answer the following question: *Is the relationship between $\bar{q}_l$ and C_s independent of the cloud regime and the horizontal-averaging distance?* Figure 8 is presented to address the first part of the question. The second part of the question will be addressed in section 4d. The high correlation between $\bar{q}_l$ and C_s also appears in the ASTEX simulation, that is, between 0.86 and 0.97 at four selected levels. More importantly, such a high correlation also appears in the observational data (0.87; Fig. 8e). Figure 8e is similar to Fig. 3b except that the LWP is divided by the difference of cloud-top and cloud-base heights and air density that were also observed by White et al. (1995). These results suggest that such a relationship between $\bar{q}_l$ and C_s is not significantly dependent on simulated cloud regimes.

c. Effect of horizontal inhomogeneity on C_s

Three variables are used to measure the horizontal inhomogeneity of subgrid-scale circulations: (i) cloud mass flux per unit area M_c, (ii) cloud-scale vertical kinetic energy (CKE), and (iii) parameterized turbulent kinetic energy (TKE) in the stratiform regions. Here M_c is defined as the horizontal integral of the product of vertical mass flux and fractional cloud area at a specific level in the stratiform regions. The subdomain averaged vertical motion is excluded in M_c. That is, the convective circulations are horizontally homogeneous within the cloudy grids if $M_c = 0$. CKE and TKE measure the horizontal inhomogeneity of all grids in the stratiform regions, although they represent different scales of motion.

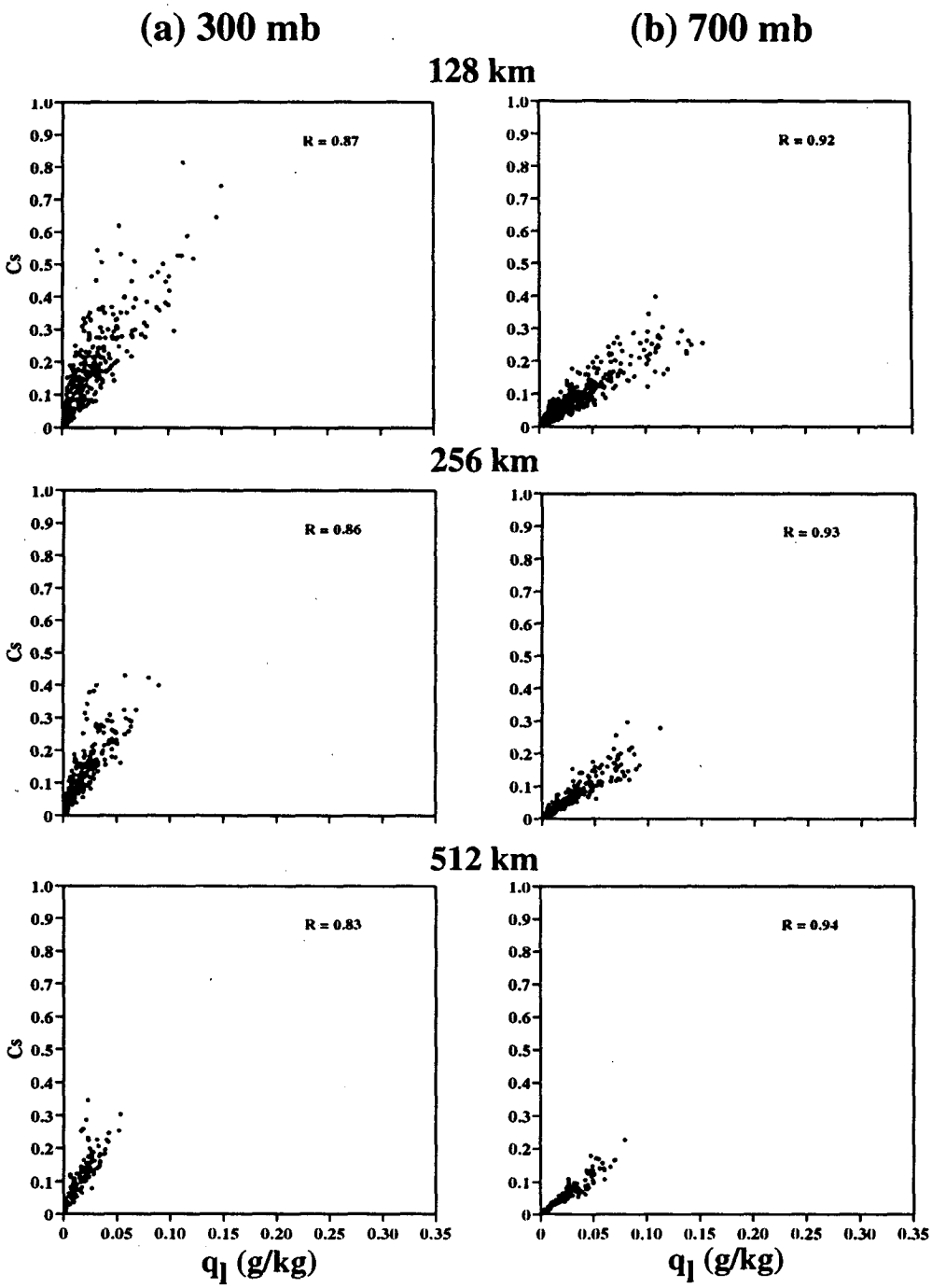

FIG. 10. Same as Fig. 7 except for the 128-, 256-, and 512-km subdomains at (a) 300-mb and (b) 700-mb levels.

Figure 9a indicates that the averaged intensity of convective circulations in the stratiform regions increases as C_s decreases. That is, large C_s is generally associated with small M_c. This suggests that the horizontal inhomogeneity of convective circulations tends to reduce C_s. Neither CKE nor TKE is as well correlated with C_s as $\bar{q}_l$ or RH (Figs. 9b and 9c). Although the range of variations in TKE is larger than that in CKE, the correlation between TKE and C_s is slightly higher than that between CKE and C_s in the lower and middle troposphere. A negative correlation between CKE and C_s does not exist because CKE will not be

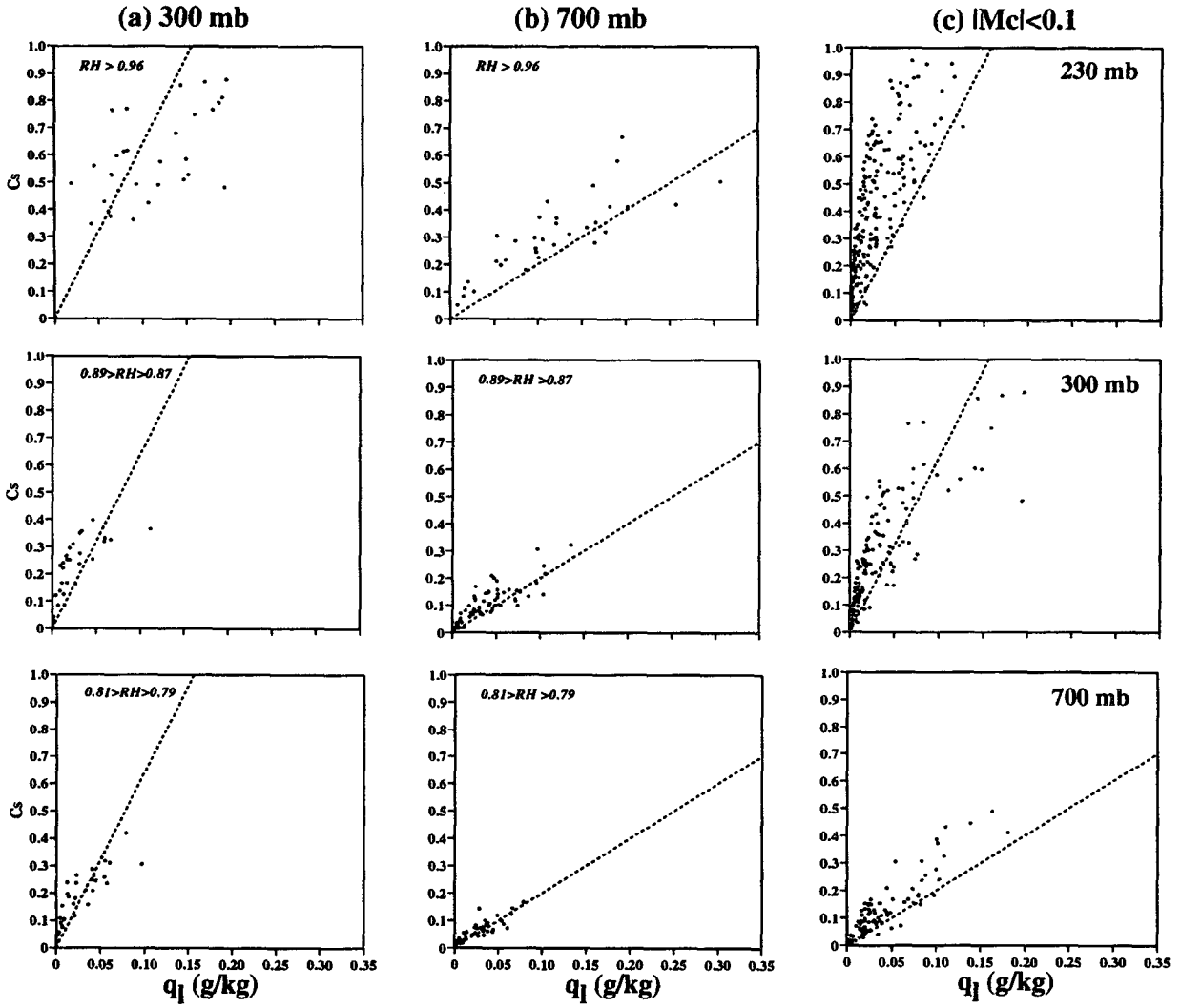

FIG. 11. Same as Fig. 7 except for showing the dependency of the C_s vs $\bar{q}_l$ relationship on RH at (a) 300-mb and (b) 700-mb levels and, (c) the dependency on cloud mass flux at 230-, 300-, and 700-mb levels. The dashed lines are the linear regressions of the whole dataset shown in Fig. 7.

zero for a perfectly homogeneous cloudy layer if C_s is less than 1. This is due to the subsidence in the clear regions.

Another related issue is whether or not C_s is a result of detrainment of cloudy air from cumulus towers. In other words, is updraft mass flux in convective regions well correlated with C_s? The answer is not affirmative by the simulated data. The correlation coefficients between C_s and updraft mass flux in convective regions are significantly positive (0.4–0.7) below 900 mb and above 300 mb, but small positive (0.1–0.3) or slightly negative for levels between 300 and 800 mb for all horizontal-averaging distances between 64 and 512 km (Table 1). That is, C_s is somewhat associated with updraft mass flux in convective regions. The correlation coefficients between C_s and total mass flux in stratiform regions are relatively small in the lower troposphere, where stratiform cloudiness is small, but are much larger in the middle upper troposphere, where stratiform cloudiness is large (Table 1). These results suggest that C_s is associated with both the local production of condensate due to mesoscale lifting and the detrainment of cloudy air from cumulus tower, which agrees somewhat with observations of Leary and Houze (1980). On the other hand, the present results suggest that the local production of condensate is far more dominant than the detrainment in the middle upper troposphere, while the detrainment is mostly dominant in the high upper troposphere. The relative importance of local production to detrainment processes decreases as the horizontal-averaging distance increases (Table 1).

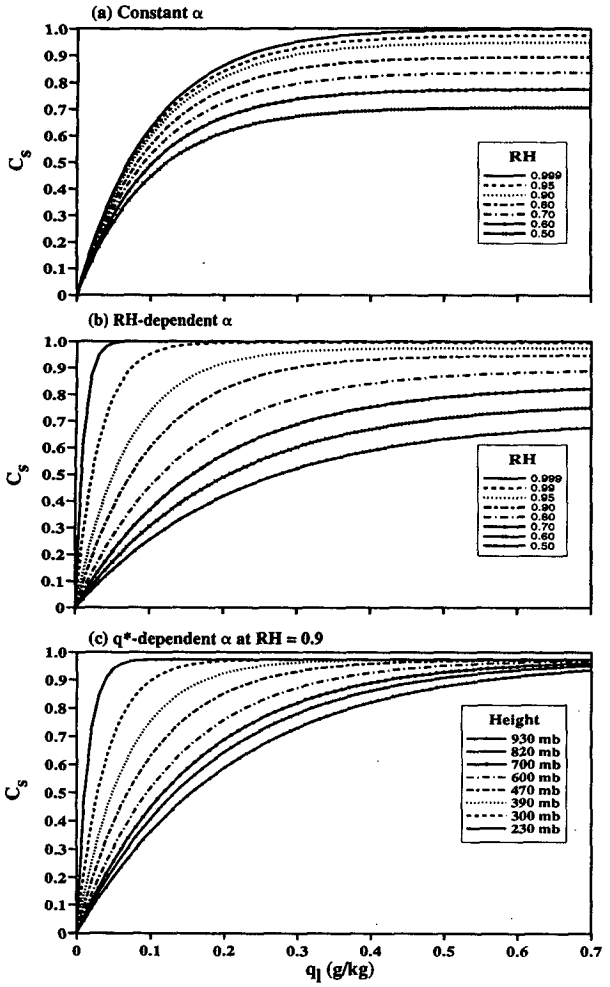

FIG. 12. The proposed parameterization of cloud fraction under three different assumptions on the slope parameter α. See text for explanation.

d. *Independence of horizontal-averaging distance*

Figure 10 shows scatter plots for the 128-km, 256-km and 512-km subdomain averages at the 300-mb and 700-mb levels. Results from these two levels are shown because the range of C_s variations is large. As far as the correlation coefficients between $\bar{q}_l$ and C_s and the slopes of the regression lines at a given level are concerned, there is no significant difference among the different subdomain averages (see Figs. 7b and 7f for the 64-km subdomain). Therefore, the relationship between $\bar{q}_l$ and C_s is basically independent of the subdomain size in the range of 64 km to 512 km. As expected, there is greater scatter for smaller subdomain sizes due to the presence of fewer clouds in the subdomain averaging. That is, the average for C_s and $\bar{q}_l$ in the large subdomains includes a sufficiently large number of clouds that could give a statistically complete distribution of cloud water/ice on the subgrid scale. Another reason is that variations of domain-averaged RHs in large subdomains are smaller, which affects the slope of C_s versus $\bar{q}_l$, as shown below.

e. *Interrelationships among predictors*

It is apparent that $\bar{q}_l$ alone cannot give an accurate estimate of C_s because there is significant scatter of C_s for a given $\bar{q}_l$. A straightforward question is *what causes the scatter in the relationship between* $\bar{q}_l$ *and* C_s*?* Other related questions are *what determines the slope of the* C_s *variation with respect to* $\bar{q}_l$, and *what determines the maximum* C_s *for large* $\bar{q}_l$*?* To address these questions, data used in $\bar{q}_l$ versus C_s plots are stratified according to the grid-averaged RH and cloud mass flux M_c, respectively.

Figures 11a and 11b show data with selected RH ranges at the 300-mb and 700-mb levels for the 64-km subdomains. Results from other levels are similar (not shown). The main feature in Figs. 11a and 11b is that data with higher (lower) RHs appear in the upper (lower) portion of the scatterplots; that is, C_s increases as RH increases for a given $\bar{q}_l$. However, the scatter is still large for large RHs. For small RHs, scatter points are concentrated on the left portion of the plot because $\bar{q}_l$ cannot be large when RH is low. If each subset of the data is treated separately, the slope of the regression line is far steeper for that with large RHs. (Note that the slope becomes less steep for very large $\bar{q}_l$.) This suggests that RH is a major factor for determining the slope of the C_s variation with respect to $\bar{q}_l$. Thus, results shown above indicate that RH should also be used as a predictor for C_s.

The large scatter is not just dependent upon the RH. The intensity of convective circulations in the stratiform regions is also a contributing factor for determining the slope of the C_s variation with $\bar{q}_l$ (Fig. 11c). Obviously, the slope is far steeper for small M_c than for large M_c (compare with Fig. 7). This is not a surprising result because horizontal inhomogeneity tends to reduce C_s for given $\bar{q}_l$ and RH. It is also apparent that although M_c is a secondary predictor for C_s, it is far less significant than RH.

5. A proposed parameterization

Based on the understanding of the relationships between C_s and its predictors discussed above, an intuitive formulation can be proposed as follows:

$$C_s = \mathrm{RH}^p[1 - \exp(-\alpha \bar{q}_l)], \qquad (1)$$

where p and α are nondimensional coefficients to be determined. It can be seen from (1) that C_s will gradually approach its upper limit as $\bar{q}_l$ increases. This limit is 1 for RH = 1. Note that p and α must be positive. Otherwise, C_s would exceed 1. Figure 12a shows the dependency of

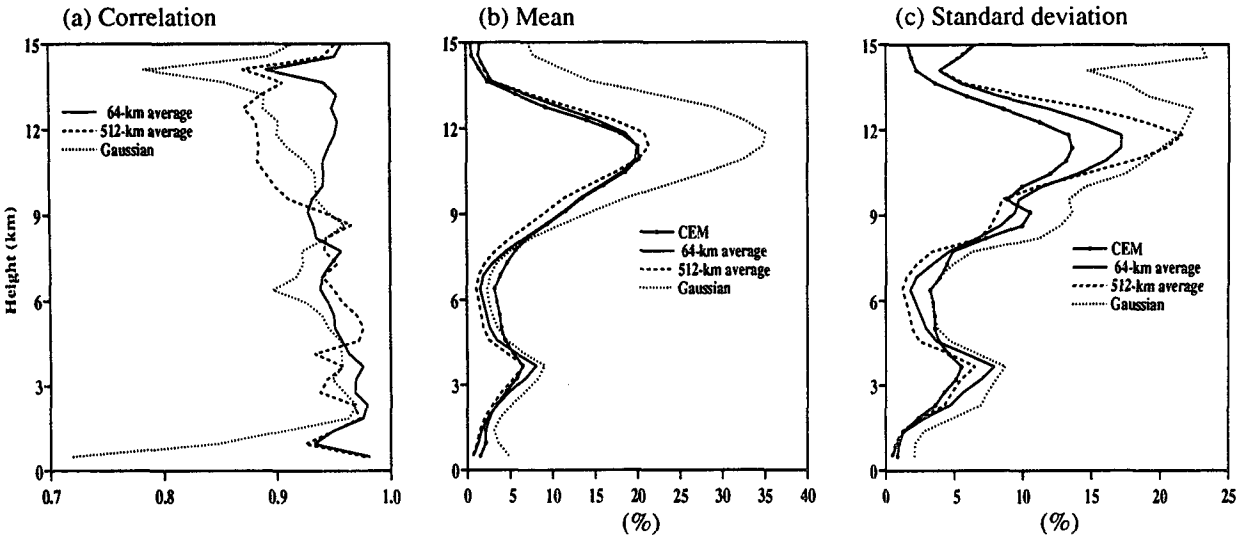

FIG. 13. Vertical profiles of (a) the correlation coefficient between simulated and parameterized cloud amounts, (b) the mean, and (c) the standard deviation. The parameterized cloud amounts include those with 64-km and 512-km subdomain-averaged inputs and that with the Gaussian model using the 512-km domain-averaged input.

C_s on RH and $\bar{q}_l$, where p and α are chosen to be 0.5 and 10^4, respectively. The value of α is at least twice as great as that being inferred from Figs. 7 and 8 so that the dependency of C_s on $\bar{q}_l$, to some extent, resembles those shown in Figs. 7 and 8. It is apparent that the slopes of the curves with large RHs in Fig. 12a are not as steep as those shown in Figs. 7, 8, and 11 when $\bar{q}_l$ is small. It should be pointed out that the dependency of C_s on M_c is not considered in (1) since M_c is not available in most climate models. Note that M_c here is the convective mass flux in stratiform regions.

Another feature in (1) is related to the derivative of C_s with $\bar{q}_l$; that is,

$$\partial C_s/\partial \bar{q}_l = \mathrm{RH}^p \alpha \exp(-\alpha \bar{q}_l). \qquad (2)$$

When condensation begins to occur ($\bar{q}_l \approx 0$), this derivative depends only upon $\mathrm{RH}^p\alpha$. That is, a larger C_s can be formed in a grid cell with a higher RH. It is apparent that the physics behind (1) is fundamentally different from existing parameterizations based on RH alone because RH is here used to determine the slope of the variation between C_s and $\bar{q}_l$. Furthermore, (2) indicates that $\partial C_s/\partial \bar{q}_l$ becomes smaller at a given RH as $\bar{q}_l$ increases. This is well supported by the results discussed in section 4e (Figs. 11a and 11b).

If α is assumed to be independent of RH, p has to approach the order of 10 so that the dependency of C_s on RH at a given $\bar{q}_l$ can be accounted for. For example, C_s at 99% RH is twice that at 88% RH at $\bar{q}_l = 0.1$ g kg^{-1} of the 300-mb level (Fig. 11a). The derived p is 17 [2/log(0.99/0.88)]. A similar argument for the 700-mb level (Fig. 11b) would result in a slightly smaller p. This difference will be explained later. At any rate, such a strong dependency on RH is not physically realistic. Therefore, we assume that α is also a function of RH, that is, when RH is close to 1, C_s increases rapidly with $\bar{q}_l$.

In Fig. 12b, α is assumed to be $\alpha_0(1 - \mathrm{RH})^p$, where α_0 is chosen so that the curves with RH = 0.9 are identical between Figs. 12a and 12b. It is apparent that the curves with RH greater than 0.9 in Fig. 12b have much steeper slopes than those in Fig. 12a; that is, C_s becomes 1 for a very small $\bar{q}_l$ when RH is close to 1. This is what one would expect from simple physical intuition. Another difference between Figs. 12a and 12b is that C_s is more strongly dependent upon RH for small $\bar{q}_l$. This can explain the dependency of C_s on RH examined in section 4e.

On the other hand, it is more appropriate that α is a function of saturation deficiency. This accounts for the steeper slopes of C_s versus $\bar{q}_l$ in the upper troposphere (Fig. 7) since saturation deficiency is proportional to the saturation water vapor mixing ratio q^*. Thus,

$$\alpha = \alpha_0[(1 - \mathrm{RH})q^*]^{-\gamma}, \qquad (3)$$

where γ should be positive and α_0 is a constant. This implies that C_s becomes 1 as RH approaches 1. Of course, when RH $\geq$ 1 in a grid cell, a 100% cloud amount is assumed. The rapid increase of C_s with respect to $\bar{q}_l$ at very high RHs, as shown in Figs. 11a and 11b, can therefore be captured by (3). In summary, the new parameterization can be written as

$$C_s = \begin{cases} \mathrm{RH}^p[1 - \exp(-\alpha_0 \bar{q}_l / [(1 - \mathrm{RH})q^*]^{\gamma})], & \text{if } \mathrm{RH} < 1 \\ 1, & \text{if } \mathrm{RH} \geq 1. \end{cases} \qquad (4)$$

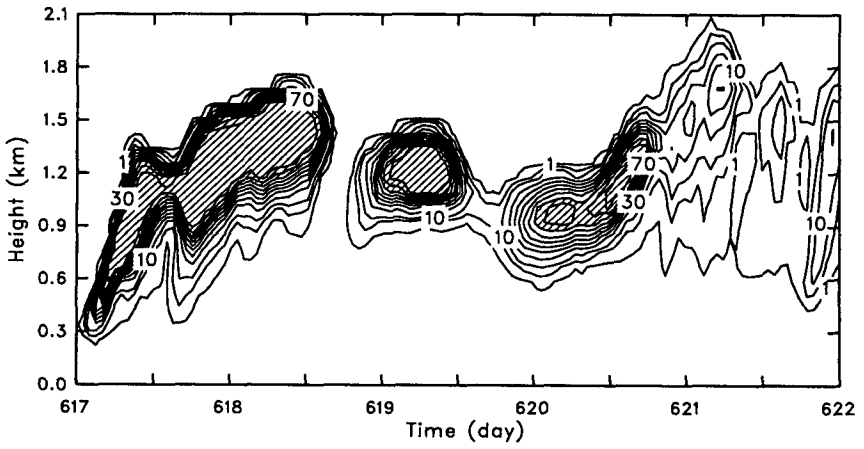

FIG. 14. Same as Fig. 2a except for the parameterized cloud fraction.

Figure 12c shows the dependency of C_s on q^* with RH = 0.9 for the proposed parameterization. The slopes of C_s versus $\overline{q_l}$ are much steeper in the upper troposphere than those below the melting level because saturation mixing ratio with respect to ice is much smaller than with respect to water. Because of the steeper slope in the upper troposphere, the dependency of C_s on RH is much stronger. This can explain the results shown in Figs. 11a and 11b.

The values of p, α_0, and γ can be empirically determined from the simulated data using statistical regression for the best-fit constants. All three coefficients in the proposed parameterization are assumed to be independent of height. The determined p, γ, and α_0 values from the GATE simulation are 0.25, 0.49, and 100, respectively. The latter two are obtained by matching the mean value of the two maxima in the lower and upper troposphere (Fig. 13b). An increase (decrease) of γ with a decrease (increase) of α_0 from the optimal values gives an overestimate of the maximum in the upper (lower) troposphere. The value of p is obtained to give the least underestimate in the middle troposphere. The 512-km averaged data of the GATE simulation are only used to obtain these constants. Note that these constants could be sensitive to the underestimate of simulated low-level cloudiness discussed in section 2a.

Figure 13 shows an evaluation of the proposed parameterization and is comparable to the prediction by the Gaussian PDF model (see Xu and Randall 1996b). The new parameterization does not have the large overestimate in the upper troposphere as the Gaussian model for the 512-km average. The evaluation with the 64-km average was done by averaging the predicted C_s over the eight subdomains to obtain the mean C_s for the entire domain. The 64-km average result is slightly better than that of the entire domain because of the wider range of variations in the predictors. Similar results appear in the 128-km and 256-km subdomains (not shown). All of these strongly suggest that the parameterization is independent of horizontal-averaging distance, at least in the range of 64–512 km.

Figure 14 gives an independent evaluation of the new parameterization with the ASTEX simulation. The time–height distribution of parameterized cloud fraction is similar to that simulated (Fig. 2a) except for slight overestimates during a few periods. This suggests that the parameterization may not strongly depend on cloud regimes. Further evaluation of this parameterization is needed with datasets of other cloud regimes.

6. Discussion and conclusions

In this study, data produced from explicit simulations of observed tropical cloud systems during GATE and subtropical stratocumuli during ASTEX have been used to develop a framework for empirically parameterizing stratiform cloudiness for climate models.

A major contribution of the present study is to propose a semi-empirical cloudiness parameterization based on consideration of the relationships between stratiform cloud amount and its large-scale predictors. The idea can be summarized as follows. The grid-averaged mixing ratio of condensate (cloud water and cloud ice) is a much better predictor for stratiform cloudiness than the grid-averaged RH. The degree of variation between cloud amount and grid-averaged mixing ratio of condensate is also dependent upon RH and the convective circulations within stratiform regions. Therefore, this parameterization uses the grid-averaged condensate mixing ratio as the primary predictor. The grid-averaged RH and convective mass flux are also used in the parameterization but as secondary predictors. Briefly, the cloud amount is assumed to vary exponentially with the grid-averaged condensate mixing ratio. The rate of variation is, however, a function of grid-averaged RH and the intensity of convective circulations, as expressed by (4). (The latter has not

been considered in the present version of the proposed formulation.)

The validity of such a semi-empirical approach and its dependence on cloud regime and horizontal-averaging distance have also been explored with the simulated datasets.

An advantage of the proposed parameterization is that it does not require information on the high-order moments, which are needed in PDF-based parameterizations (Xu and Randall 1996b). It can be applied in climate models with a prognostic approach for cloud formation and dissipation processes in which the grid-averaged mixing ratio of condensates is predicted. It uses the grid-averaged RH differently from most existing parameterizations and may be more physically realistic. The formulation is independent of the grid size of climate models, at least in the range of 64–512 km. Its independency on cloud regimes needs to be further evaluated with additional simulations of other cloud regimes. Its possible dependency on layer thickness is yet to be examined because the probability distribution of cloud thickness in this study is idealized to "cloud" and "cloud free." A more general parameterization of cloud fraction is left for the future.

A direct evaluation of this parameterization from observations will be attempted in the near future using data from the Atmospheric Radiation Measurement Program (Stokes and Schwartz 1994) and other field experiments. An indirect evaluation can be done by checking the realism of the simulation. For example, the frequency distribution of the liquid/ice water path from each CEM grid column can be compared with that from fine pixels of satellite observations over the oceans (Harshvardhan et al. 1994). Other statistical properties of cloud ensembles from observations can also be compared with simulations (see Xu and Randall 1995a). Further evaluation and testing of this parameterization will be performed in a climate model. A preliminary test of this parameterization was performed at ECHAM GCM (Lohmann and Roeckner 1996). Their results with this parameterization are better in the Tropics than with an RH-type parameterization. Additional simulations with different large-scale conditions will be performed to refine the proposed parameterization.

Acknowledgments. This research was primarily supported by the Environmental Sciences Division of the U.S. Department of Energy under Grant DE-FG03-95ER61968 as part of the Atmospheric Radiation Measurement Program. It was also partially supported by CERES under Grant NAG1-1266 and FIRE under Grant NAG1-1701, both from NASA to the Colorado State University.

Observational datasets used in the present study were kindly provided by Professor R. Reed of the University of Washington and Professor M. Yanai of UCLA for the GATE sounding data, Professor C. Bretherton of the University of Washington for the ASTEX data, Mr. R. Holle of NOAA NSSL for the GATE whole-sky cloudiness data, and Dr. A. White of NOAA ETL for the ASTEX cloudiness data. We are grateful to Professor A. Arakawa and two anonymous reviewers for their constructive comments, Tammy Weckwerth for improving the manuscript, and Bruce Wielicki and Steve Krueger for their interest in this work.

REFERENCES

Albrecht, B. A., 1981: Parameterization of trade cumulus cloud amounts. *J. Atmos. Sci.*, **38,** 97–105.

——, M. P. Jensen, and W. J. Syrett, 1995a: Marine boundary layer structure and fractional cloudiness. *J. Geophys. Res.*, **100,** 14 209–14 222.

——, C. S. Bretherton, D. Johnson, W. H. Schubert, and A. S. Frisch, 1995b: The Atlantic Stratocumulus Transition Experiment—ASTEX. *Bull. Amer. Meteor. Soc.*, **76,** 889–904.

Bretherton, C. S., E. Klinker, A. K. Betts, and J. A. Coakley Jr., 1995: Comparison of ceilometer, satellite, and synoptic measurements of boundary-layer cloudiness and the ECMWF diagnostic cloud parameterization scheme during ASTEX. *J. Atmos. Sci.*, **52,** 2736–2751.

Chen, J.-M., 1991: Turbulence-scale condensation parameterization. *J. Atmos. Sci.*, **48,** 1510–1512.

Fowler, L. D., D. A. Randall, and S. A. Rutledge, 1996: Liquid and ice cloud microphysics in the CSU general circulation model. Part I: Model description and simulated microphysical processes. *J. Climate,* **9,** 489–529.

Ghan, S. J., and R. C. Easter, 1992: Computationally efficient approximations to stratiform cloud microphysics parameterization. *Mon. Wea. Rev.*, **120,** 1572–1582.

Grabowski, W. W., and P. K. Smolarkiewicz, 1990: Monotone finite-difference approximations to the advection–condensation problem. *Mon. Wea. Rev.*, **118,** 2082–2097.

Gregory, D., and M. J. Miller, 1989: A numerical study of the parameterization of deep tropical convection. *Quart. J. Roy. Meteor. Soc.*, **115,** 1209–1241.

Harshvardhan, R. Davies, D. A. Randall, and T. G. Corsetti, 1987: A fast radiation parameterization for general circulation models. *J. Geophys. Res.*, **92,** 1009–1016.

——, B. A. Wielicki, and K. M. Ginger, 1994: The interpretation of remotely sensed cloud properties from a model parameterization perspective. *J. Climate,* **7,** 1987–1998.

Holle, R. L., J. Simpson, and S. W. Leavitt, 1979: GATE B-scale cloudiness from whole-sky cameras on four U.S. ships. *Mon. Wea. Rev.*, **107,** 874–895.

Houze, R. A., Jr., 1977: Structure and dynamics of a tropical squall-line system. *Mon. Wea. Rev.*, **105,** 1540–1567.

Krueger, S. K., 1988: Numerical simulation of tropical cumulus clouds and their interaction with the subcloud layer. *J. Atmos. Sci.*, **45,** 2221–2250.

——, Q. Fu, K. N. Liou, and H.-N. Chin, 1995: Improvements of an ice-phase microphysics parameterization for use in numerical simulations of tropical convection. *J. Appl. Meteor.*, **34,** 281–287.

Leary, C. A., and R. A. Houze Jr., 1980: The contribution of mesoscale motions to the mass and heat fluxes of an intense tropical convective system. *J. Atmos. Sci.*, **37,** 784–796.

LeTreut, H., and Z.-X. Li, 1988: Using meteosat data to validate a prognostic cloud generation scheme. *Atmos. Res.*, **21,** 273–292.

Lin, Y.-L., R. D. Farley, and H. D. Orville, 1983: Bulk parameterization of the snow field in a cloud model. *J. Climate Appl. Meteor.*, **22,** 1065–1092.

Lohmann, U., and E. Roeckner, 1996: Introduction of a new cloud cover parameterization in the ECHAM general circulation model. *Second Int. Scientific Conf. on the Global Energy and Water Cycle.* Washington, DC, U.S. National Academy of Sciences, 394–395.

Lord, S. J., H. E. Willoughby, and J. M. Piotrowicz, 1984: Role of a parameterized ice-phase microphysics in an axisymmetric, nonhydrologic tropical cyclone model. *J. Atmos. Sci.*, **41,** 2836–2848.

Randall, D. A., 1987: Turbulent fluxes of liquid water and buoyancy in partly cloudy layers. *J. Atmos. Sci.*, **44,** 850–858.

——, 1989: Cloud parameterization for climate modeling: Status and prospects. *Atmos. Res.*, **23,** 345–361.

——, J. A. Coakley Jr., C. W. Fairall, R. A. Kropfli, and D. H. Lenschow, 1984: Outlook for research on subtropical marine stratiform clouds. *Bull. Amer. Meteor. Soc.*, **65,** 1290–1301.

——, Harshvardhan, D. A. Dazlich, and T. G. Corsetti, 1989: Interactions among radiation, convection, and large-scale dynamics in a general circulation model. *J. Atmos. Sci.*, **46,** 1943–1970.

Slingo, J. M., 1980: A cloud parameterization scheme derived from GATE data for use with a numerical model. *Quart. J. Roy. Meteor. Soc.*, **106,** 747–770.

——, 1987: The development and verification of a cloud prediction scheme for the ECMWF model. *Quart. J. Roy. Meteor. Soc.*, **113,** 899–927.

Smagorinsky, J., 1960: On the dynamical prediction of large-scale condensation by numerical methods. *Physics of Precipitation, Geophys. Monogr.*, No. 5, Amer. Geophys. Union, 71–78.

Smith, R. N. B., 1990: A scheme for predicting layer clouds and their water content in a GCM. *Quart. J. Roy. Meteor. Soc.*, **116,** 435–460.

Stokes, G. M., and S. E. Schwartz, 1994: The Atmospheric Radiation Measurement (ARM) program: Programmatic background and design of the cloud and radiation test bed. *Bull. Amer. Meteor. Soc.*, **75,** 1202–1221.

Sundqvist, H., 1978: A parameterization scheme for non-convective condensation, including prediction of cloud water content. *Quart. J. Roy. Meteor. Soc.*, **104,** 677–690.

Tao, W.-K., J. Simpson, and S.-T. Soong, 1987: Statistical properties of a cloud ensemble: A numerical study. *J. Atmos. Sci.*, **44,** 3175–3187.

Tiedtke, M., 1993: Representation of clouds in large-scale models. *Mon. Wea. Rev.*, **121,** 3040–3061.

Walcek, C. J., 1994: Cloud cover and its relationship to relative humidity during a springtime midlatitude cyclone. *Mon. Wea. Rev.*, **122,** 1021–1035.

Webster, P. J., and G. L. Stephens, 1980: Tropical upper-troposphere extended clouds: Inferences from Winter MONEX. *J. Atmos. Sci.*, **37,** 1521–1541.

White, A. B., C. W. Fairall, and J. B. Snider, 1995: Surface-based remote sensing of marine boundary-layer cloud properties. *J. Atmos. Sci.*, **52,** 2827–2838.

Xu, K.-M., 1995: Partitioning mass, heat, and moisture budgets of explicitly simulated cumulus ensembles into convective and stratiform components. *J. Atmos. Sci.*, **52,** 551–573.

——, and S. K. Krueger, 1991: Evaluation of cloudiness parameterizations using a cumulus ensemble model. *Mon. Wea. Rev.*, **119,** 342–367.

——, and D. A. Randall, 1995: Impact of interactive radiative transfer on the macroscopic behavior of cumulus ensembles. Part I: Radiation parameterization and sensitivity test. *J. Atmos. Sci.*, **52,** 785–799.

——, and ——, 1996a: Explicit simulation of cumulus ensembles with the GATE Phase III data: Comparison with observations. *J. Atmos. Sci.*, in press.

——, and ——, 1996b: Evaluation of statistically based cloudiness parameterizations used in climate models. *J. Atmos. Sci.*, **53,** 3103–3119.

——, A. Arakawa, and S. K. Krueger, 1992: The macroscopic behavior of cumulus ensembles simulated by a cumulus ensemble model. *J. Atmos. Sci.*, **49,** 2404–2420.